

# Blind Estimation of the Arterial Input Function in Dynamic Contrast-Enhanced MRI Using Purity Maximization

Yu-Chun Lin,<sup>1–3</sup> Tsung-Han Chan,<sup>4</sup> Chong-Yung Chi,<sup>4</sup> Shu-Hang Ng,<sup>1,3,5</sup> Hao-Li Liu,<sup>2,5</sup> Kuo-Chen Wei,<sup>6</sup> Yau-Yau Wai,<sup>1,3</sup> Chun-Chieh Wang,<sup>3,7</sup> and Jiun-Jie Wang<sup>1,3\*</sup>

**Uncertainty in arterial input function (AIF) estimation is one of the major errors in the quantification of dynamic contrast-enhanced MRI. A blind source separation algorithm was proposed to determine the AIF by selecting the voxel time course with maximum purity, which represents a minimal contamination from partial volume effects. Simulations were performed to assess the partial volume effect on the purity of AIF, the estimation accuracy of the AIF, and the influence of purity on the derived kinetic parameters. In vivo data were acquired from six patients with hypopharyngeal cancer and eight rats with brain tumor. Results showed that in simulation the AIF with the highest purity is closest to the true AIF. In patients, the manually selection had reduced purity, which could lead to underestimations of  $K^{\text{trans}}$  and  $V_e$  and an overestimation of  $V_p$  when compared with those obtained by the proposed blind source separation algorithm. The derived kinetic parameters in the tumor were more susceptible to the changes in purity when compared with those in the muscle. The animal experiment demonstrated good reproducibility in blind source separation-AIF derived parameters. In conclusion, the blind source separation method is feasible and reproducible to identify the voxel with the tracer concentration time course closest to the true AIF. Magn Reson Med 000:000–000, 2012. © 2012 Wiley Periodicals, Inc.**

**Key words:** dynamic contrast-enhanced MRI; arterial input function; pharmacokinetic modeling

Dynamic contrast-enhanced magnetic resonance imaging (DCE-MRI) is a noninvasive imaging tool for estimation

of tissue physiological parameters, such as perfusion, capillary permeability, and the volume of extravascular–extracellular space. The interest in these parameters arises because they were shown to be related to the response of therapy and the overall survival time [1–3]. The conventional practice of the quantitative analysis was by fitting the time course of the enhancement pattern immediately after contrast agent injection with a pharmacokinetic model. Since the pharmacokinetic model requires the knowledge of the arterial input function (AIF), which describes the temporal evolution of the contrast agent concentration in the blood pool [4–6], the accuracy of the derived kinetic parameters largely depends on measurement of the AIF.

The estimation of AIF remains a main challenge in DCE-MRI [7,8]. Manual selection of an artery of interest requires the successful identification of a large vessel within the field of view. It is apparently subjective, operator-dependent and susceptible to partial volume artifacts, which potentially could lead to significant errors in the subsequent estimation of the pharmacokinetic parameters [9]. Alternatively, Parker et al. developed a population-averaged AIF [10], which is simple and convenient for clinical use. However, it is possible to introduce artifactual changes in kinetic modeling parameters if systemic circulatory factors, such as cardiac or renal function, are altered due to an intervention. The reference region approach extracted the AIF by comparing the measured data in healthy tissues with the literature values. It was limited by the requirement of a well-characterized normal tissue within the field of view [11–13].

Blind source separation (BSS) is an approach to estimate the underlying source signals from the mixtures without a priori knowledge about the mixing process, and therefore can be a method to automatically estimate AIF. Independent component analysis is a representative BSS technique that has been previously proposed for the AIF estimation [14]. However, all the source signals are assumed to be statistically independent, which could be invalid in DCE-MRI data because the tracer concentrations of all the pixels in a tissue are relevant due to similar-behaved blood supplies from the common circulation system, subject to potential time delays and dispersions. Fluckiger et al. used the iterative quadratic maximum likelihood (IQML) algorithm to fit the estimated AIF using a novel model that comprises two normalized  $\gamma$ -variant curves to minimize the effect of noise [15,16]. It does not require such statistical assumptions. However,

<sup>1</sup>Department of Medical Imaging and Intervention, Chang Gung Memorial Hospital, Linkou, Taiwan.

<sup>2</sup>Department of Electrical Engineering, Chang Gung University, Taoyuan, Taiwan.

<sup>3</sup>Department of Medical Imaging and Radiological Science, Chang Gung University, Taoyuan, Taiwan.

<sup>4</sup>Institute of Communications Engineering and Department of Electrical Engineering, National Tsing Hua University, Hsinchu, Taiwan.

<sup>5</sup>Molecular Imaging Center, Chang Gung Memorial Hospital, Linkou, Taiwan.

<sup>6</sup>Department of Neurosurgery, Chang Gung University College of Medicine and Memorial Hospital, Taoyuan, Taiwan.

<sup>7</sup>Department of Radiation Oncology, Chang Gung Memorial Hospital, Linkou, Taiwan.

Additional Supporting Information may be found in the online version of this article.

Grant sponsor: National Science Council (R.O.C.); Grant numbers: NSC-100-2314-B-182-024, NSC 99-2221-E-007-003-MY3; Grant sponsor: Chang-Gung Memorial Hospital; Grant number: CMRPG3A0931.

\*Correspondence to: Jiun-Jie Wang, Department of Medical Imaging and Radiological Sciences, Chang Gung University, 259 Wen-Hwa, 1st Road, Kwei-Shan, Taoyuan, Taiwan. E-mail: jwang@mail.cgu.edu.tw

Received 8 August 2011; revised 5 December 2011; accepted 9 December 2011.

DOI 10.1002/mrm.24144

Published online in Wiley Online Library (wileyonlinelibrary.com).

© 2012 Wiley Periodicals, Inc.

the solution of IQML that involves dealing with the non-convex problem can be prone to initializations.

In this study, we proposed a fully data-driven BSS algorithm that could estimate AIF from individuals without any presumed AIF model and initialization. The purity of each voxel time course is a physical reflection of the contamination by the mixed tissue components in a single voxel. Increased purity of the voxel of interest could be related to a decreased partial volume effect. The AIF can be extracted from the time course of voxels with the maximum purity in the mixed tissue concentration. Monte-Carlo simulations were performed to evaluate the influence of AIF purities on the kinetic parameters and the noise sensitivity of the BSS-AIF method. The kinetic parameters derived from both BSS and manually selected AIFs were compared from six patients with hypopharyngeal cancer. The reproducibility was assessed using eight rats with brain tumors by repeated acquisitions.

## THEORY

### BSS-Based AIF Estimation

The extended Kety model [17,18] for pharmacokinetic analysis was adopted. The time-dependent concentration of the contrast agent in a tissue voxel at time is as follows:

$$C_t(t_k) = K^{\text{trans}} \sum_{n=1}^k \Delta t C_p(t_n) \times \exp[-k_{\text{ep}}(t_k - t_n)] + V_p C_p(t_k), \quad k = 1, \dots, K, \quad (1)$$

where  $C_p(t_k)$  is the tracer concentration in the blood plasma, i.e. the AIF,  $C_t(t_k)$  is the tracer concentration in the tissue,  $K^{\text{trans}}$  and  $k_{\text{ep}} (= K^{\text{trans}}/V_e)$  are the transfer rate constant from the intravascular system to the extravascular-extracellular space and that from the extravascular-extracellular space to the intravascular system, respectively,  $V_p$  and  $V_e$  are the capillary plasma volume and the distribution volume of contrast agent in the extravascular-extracellular space (per unit volume of tissue), respectively,  $\Delta t$  is the temporal resolution, and  $K$  is the total number of DCE-MRI image time series.

The notation  $i$  is introduced to generalize Eq. 1 for different voxels; for instance,  $C_t(t_k, i)$  is the tracer concentration for time  $t_k$  and voxel  $i$ , and  $K^{\text{trans}}(i)$ ,  $k_{\text{ep}}(i)$ ,  $V_e(i)$  and  $V_p(i)$  are the associated kinetic parameters for the voxel  $i$ . Note that the AIF  $C_p(t_k)$  is independent of voxel location. By collecting all the  $C_t(t_1, i) \dots C_t(t_K, i)$  into a  $K \times 1$  vector and by letting  $\mathbf{c}_p = [C_p(t_1), \dots, C_p(t_K)]^T$ , the concentration time course from a voxel of interest  $\mathbf{x}(i)$  can be given by Eq. 2

$$\mathbf{x}(i) = \begin{bmatrix} C_t(t_1, i) \\ \vdots \\ C_t(t_K, i) \end{bmatrix} = \mathbf{A}(k_{\text{ep}}(i), \mathbf{c}_p) \mathbf{s}(i), \quad [2]$$

where

$$\mathbf{s}(i) = \begin{bmatrix} K^{\text{trans}}(i) \\ V_p(i) \end{bmatrix}$$

is a vector comprising the associated (non-negative) kinetic parameters, and

$$\mathbf{A}(k_{\text{ep}}(i), \mathbf{c}_p) = \begin{bmatrix} \Delta t C_p(t_1) & C_p(t_1) \\ \sum_{n=1}^2 \Delta t C_p(t_n) \times \exp[-k_{\text{ep}}(i)(t_2 - t_n)] & C_p(t_2) \\ \vdots & \vdots \\ \sum_{n=1}^K \Delta t C_p(t_n) \times \exp[-k_{\text{ep}}(i)(t_K - t_n)] & C_p(t_K) \end{bmatrix}.$$

If the AIF ( $\mathbf{c}_p$ ) can be accurately estimated in advance, the kinetic parameters  $k_{\text{ep}}(i)$ ,  $K^{\text{trans}}(i)$ ,  $V_p(i)$  for all  $i$  can then be calculated by solving a non-negativity constrained curve fitting problem for Eq. 2 using the least squares method as in Eq. 3:

$$\min_{k_{\text{ep}}(i) \geq 0, \mathbf{s}(i) \geq 0} \|\mathbf{x}(i) - \mathbf{A}(k_{\text{ep}}(i), \hat{\mathbf{c}}_p) \mathbf{s}(i)\|_2, \quad [3]$$

where  $\hat{\mathbf{c}}_p$  denotes the estimated AIF;  $\|\cdot\|_2$  is the 2-norm operator and  $\geq$  component-wise inequality, respectively.

An unsupervised approach is now proposed to identify the AIF  $\mathbf{c}_p$  from a series of T1-weighted DCE-MRI data. The purity of the voxel of interest is defined as in Eq. 4, where  $\|\cdot\|_1$  is the 1-norm operator:

$$\rho_i = \frac{\|\mathbf{x}(i)\|_2}{\|\mathbf{x}(i)\|_1}. \quad [4]$$

The purity measure  $\rho_i$  is a reflection of the contribution from  $\mathbf{c}_p$  to  $\mathbf{x}(i)$ . The increased purity measure can be related to an increased contribution from  $\mathbf{c}_p$  in  $\mathbf{x}(i)$ . It can be related to a reduced extent of partial volume contamination. AIF can be identified from the voxels  $\mathbf{x}(i)$  whose purity measure is maximum (Eq. 5, details as in Appendix A):

$$\hat{\mathbf{c}}_p = \mathbf{x}(i^*) \quad [5]$$

for  $i^* = \arg_i \max_i \rho_i$ . The selected voxel  $\mathbf{x}(i^*)$  corresponds to the voxel time course with minimal partial volume contamination and thus can be regarded as an AIF estimate.

## MATERIALS AND METHODS

### Simulations

Simulations were performed by assuming a heterogeneous tissue with various concentration curves. The purity of each voxel was calculated. The ground-truth AIF was generated by using the modified population average AIF [12].

### Simulation A

To assess how the time concentration curve changes under different conditions. Simulation was performed by assuming a pure arterial voxel without partial volume effect, therefore  $V_p = 1$ ,  $V_e = 0$ , and  $K^{\text{trans}} = 0$ . Different extents of partial volume effect were introduced to the signal of the concentration curves by changing one pharmacokinetic parameter with the other two maintained.

The simulation included the following conditions: (1) decreased  $V_p$  to simulate the decreased contribution from the arterial component, (2) increased  $V_e$  to simulate the increased contribution from the extravascular component, and (3) increased  $K^{\text{trans}}$  to simulate the increased leakage from vascular component.

### Simulation B

A Monte-Carlo simulation was performed by creating 100 tissue concentration curves  $\mathbf{x}(i)$  using Eq. 2 with  $K^{\text{trans}}(i)$  uniformly distributed between  $[0, 2.2]$  ( $\text{min}^{-1}$ ),  $V_e(i)$   $[0, 1]$  and  $V_p(i)$   $[0, 1]$ , respectively. The following assessments were performed, which were summarized in the flowchart (Supporting Information, S1).

Assessment 1, the influence of purity level to the errors between the BSS- and true-AIF: Thirty tissue concentration curves  $\mathbf{x}(i)$  were randomly selected as the estimated AIFs, of which the purities were varied from 0.104 to 0.296. The root-mean-square-error (RMSE) between  $\mathbf{x}(i)$  and the ground-truth AIF  $\mathbf{c}_p$  was measured.

Assessment 2, the influence of signal-to-noise ratio (SNR) to the errors between the BSS- and true-AIF: Zero-mean white Gaussian noise was added in the tissue concentration curves  $\mathbf{x}(i)$ . The SNR was calculated as in Eq. 6:

$$\text{SNR} = \sum_{i=1}^{100} \|\mathbf{x}(i)\|^2 / (100\sigma^2 K), \quad [6]$$

where  $\sigma^2$  denotes the noise power and  $K$  is the total number of DCE-MRI image time series. For each SNR, a Monte-Carlo simulation of 1000 runs was created. A DCE-MRI data set was generated for each independent run. The IQML method was also performed for comparison (details in Appendix B). Three initialization settings for  $K^{\text{trans}}(i)$ ,  $V_e(i)$ , and  $V_p(i)$  were used to evaluate the initialization sensitivity to IQML method: (1) means of their own distributions,  $1.1 \text{ min}^{-1}$ , 0.5 and 0.5, respectively; (2) random values uniformly distributed on  $[0, 3]$ ,  $[0, 1]$ , and  $[0, 1]$ , respectively; (3) the ground-truth values. The RMSE between the estimated AIF and ground-truth AIF was then measured.

Assessment 3, the influence of purity of the estimated AIF to the derived kinetic parameters: The ground-truth AIF was used to generate various new  $\mathbf{x}(i)$  by the following parameter settings:

1.  $K^{\text{trans}}(i) \in \{0.05, 0.1, 0.25, 0.5\}$ ,  $V_e(i) = 0.2$ , and  $V_p(i) = 0.005$ ;
2.  $K^{\text{trans}}(i) = 0.15$ ,  $V_e(i) \in \{0.05, 0.1, 0.3, 0.5\}$ , and  $V_p(i) = 0.005$ ;
3.  $K^{\text{trans}}(i) = 0.15$ ,  $V_e(i) = 0.2$ , and  $V_p(i) \in \{0.005, 0.05, 0.25, 0.5\}$ .

Given the tissue concentration curves  $\mathbf{x}(i)$  and the thirty estimated  $\mathbf{c}_p$ s with various purities, the kinetic parameters  $K^{\text{trans}}(i)$ ,  $V_e(i)$ , and  $V_p(i)$ , can be derived by solving the curve fitting problem [3].

### DCE-MRI Data Acquisition

#### Patients

Six patients (mean age,  $60.5 \pm 11.6$ -year-old) with histologically proven diagnosis of hypopharyngeal or oral

pharyngeal cancer at stages of T3 or T4, were enrolled in the study. Written informed consent was obtained from all participants. The study was approved by institutional review board. DCE-MRI images were acquired by a 3 T scanner (Trio a TIM system, Siemens, Erlangen, Germany) using a 3D spoiled gradient-echo sequence with the following parameters: TR/TE = 3.5/1.13 ms,  $230 \times 230 \text{ mm}^2$  field of view,  $108 \times 128$  matrix, 4-mm section thickness, and 16 transverse sections in the volume. A spatial saturation slab was implanted inferior to the acquired region to minimize the inflow effect from the carotid arteries. Before the contrast agent administration, baseline longitudinal relaxation time ( $T_{10}$ ) values were calculated from image acquired with different flip angles ( $4^\circ$ ,  $8^\circ$ ,  $15^\circ$ , and  $25^\circ$ ). The dynamic series involved use of the same sequence with a  $15^\circ$  flip angle. After four acquisitions of the dynamic baseline scan, a standard dose (0.1-mmol/kg) of gadopentetate dimeglumine (Gd-DTPA, Magnevist, Bayer-Schering, Burgess Hill, UK) was administered by a power injector through a cannula placed in the antecubital vein at a rate of 3 mL/s and immediately followed by a saline flush. A total of 80 volumes were acquired with a temporal resolution of 3.3 s. The total acquisition time was 4 min and 24 s.

### Animal Experiments

To evaluate the in vivo reproducibility of the BSS-AIF, eight rats (Sprague-Dawley, 300–400 g) with implanted C6 tumors on the brain (9–15 days after tumor implantation) were imaged twice within a time interval of 4–8 h ( $4.81 \pm 1.46$  h). Images were acquired on a 7 T MR scanner (ClinScan, Bruker, Ettlingen Germany). All the procedures were carried out in accordance with the institution's Animal Care and Use Committee approval. Animals were anesthetized during the imaging experiment at 2–3% isoflurane. The temperature was maintained at  $37^\circ\text{C}$  with circulating warm water. Heart rate, respiration rate, and temperature were monitored during the MRI experiments. A dedicated rat holder with tooth bar and ear bars was used to fix the position of animals. To maintain the physiological status of animals, anesthesia was suspended to allow for recovery between the two scans. The rats were removed from the MRI holder and repositioned before the second acquisition. DCE-MRI data were acquired using a spoiled 3D gradient echo sequence with the following parameters: TR/TE = 2.31/0.76 ms, field of view =  $34 \times 49 \text{ mm}^2$ , slice thickness = 0.8 mm, and temporal resolution = 1.9 s. Baseline T1 values were calculated from image acquired with multiple flip angles ( $2^\circ$ ,  $5^\circ$ ,  $10^\circ$ ,  $15^\circ$ , and  $20^\circ$ ). A series of 120 dynamic scans with a flip angle of  $25^\circ$  were acquired followed a bolus of 0.1 mL of Gd-DTPA via a tail-vein catheter delivered using a dedicated syringe pump (PHD2000, Harvard apparatus, MA) with a constant infusion rate of 6 mL/min.

### Data Analysis

All the data were processed in MATLAB 7.0 (The Mathworks, Natick, MA). Signal intensities of the measured DCE-MRI data were converted into contrast agent

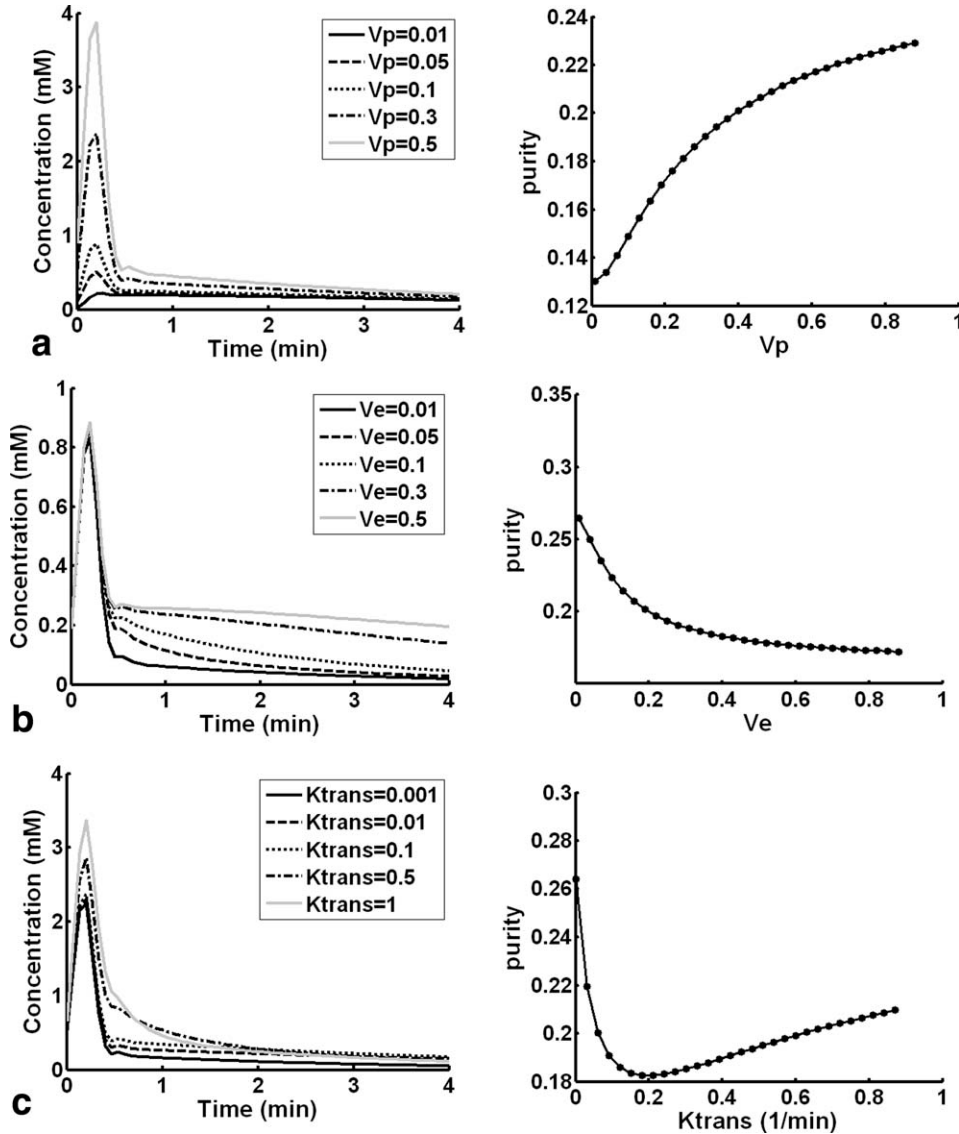


FIG. 1. Simulation A for AIFs by varying kinetic parameters of the tissue time courses (left panels) and the corresponding purity of the AIFs (right panels): (a) Varied  $V_p$  with  $V_e = 0.3$  and  $K^{\text{trans}} = 0.1$ ; (b) Varied  $V_e$  with  $V_p = 0.3$  and  $K^{\text{trans}} = 0.1$ ; (c) Varied  $K^{\text{trans}}$  with  $V_p = 0.3$  and  $V_e = 0.3$ .

concentration by solving the nonlinear relationship between the signal intensity and contrast agent concentration [19].

For each clinical data set, the AIFs were defined by both BSS-AIF and manual selection. To compare the effect from different manually selected AIFs on the derived kinetic parameters, eight tissue time courses were selected from each patient within the bilateral four arterial areas: common carotid arteries, internal carotid arteries, external carotid arteries, and vertebral arteries. The pharmacokinetic parameters,  $K^{\text{trans}}$ ,  $V_e$ , and  $V_p$ , were derived pixel by pixel using a nonlinear curve fitting to Eq. 1. Regions of interest (ROIs) within the tumor and muscle were manually delineated by an experienced radiologist based on reference images of T2 and contrast-enhanced T1-weighted images. The Spearman's rank correlations were performed on both ROIs to assess the correlations between the kinetic parameters and the corresponding purities of each AIF. The differences of the derived parameters between manual- and BSS-AIFs were calculated by Eq. 7. The correlation between the calcu-

lated difference and the purity of the corresponding AIF was assessed using Pearson's correlation. A statistical significance was reached when  $P < 0.05$ .

$$X_{\text{difference}} = |X_{\text{manual}} - X_{\text{BSS}}| / X_{\text{BSS}} \times 100\% \quad [7]$$

where  $X$  denotes the kinetic parameters  $K^{\text{trans}}$ ,  $V_e$ ,  $V_p$  and purity of AIF.

### Reproducibility Statistics

The reproducibility of the derived parameters using BSS- and manual-AIFs was examined by repeated acquisitions on the same animal. The procedure followed that as described by Padhani et al. [20–22]. All statistical tests were performed in SPSS version 12.0 (SPSS Inc., Chicago, IL), with a threshold at the 5% level of significance. ROIs were drawn on the central slice within the tumor. To make sure the clearance of the contrast media before the second acquisition, Wilcoxon's-signed rank test was used to examine the difference between the  $T1_0$

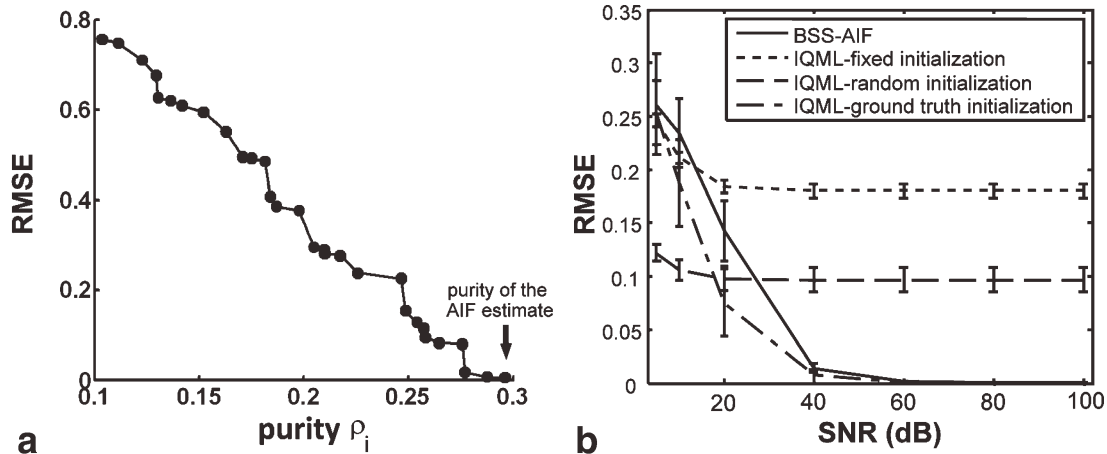


FIG. 2. Influence of purity of AIF (simulation B) and SNR to the RMSE: (a) RMSE between the ground-truth AIF and the tissue concentration curves with various purities; (b) RMSE of the AIF estimated by the proposed BSS-AIF and the IQML method (with different initializations) for various SNRs.

values of the tumor before injection. The squared root of the mean squared difference and the within-subject standard deviation was calculated between the two scans. The repeatability was assessed by a threshold below which the absolute difference between two scans of the same rat is expected to lie for 95% of pairs of observations. The within-subject coefficient of variation was used to quantify the measurement error relative to the size of the kinetic parameters. The variance ratio was calculated to compare the between-subject variance and within-subject variance for each parameter.

## RESULTS

Figure 1 plots the AIFs of the simulation A by varying kinetic parameters of the tissue concentration curves  $\mathbf{x}(i)$ . The left column shows the curves of AIF from the simulation using different  $V_p$  (a),  $V_e$  (b), and  $K^{trans}$  (c). The right panels plot the purity of the corresponding AIFs against the parameters of interest, respectively. As the  $V_p$  increased, both the peak of the AIF and the corresponding purity increased. The increase of  $V_e$  led to an ele-

vated level of the washout, and therefore the observed purity decreased. The increase of  $K^{trans}$  led to a greater area under the curve of AIF, the corresponding purity had a rapid drop to a nadir ( $\rho = 0.1825$ ,  $K^{trans} = 0.27$ ) and a subsequent slow increase to a plateau.

Figure 2 plots the results of the assessment 1 and 2 from the simulation B. Figure 2(a) plots the RMSE against the purity of the simulated AIF. As the purity of  $\mathbf{x}(i)$  increased, the RMSE between  $\mathbf{c}_p$  and  $\mathbf{x}(i)$  decreased. Figure 2(b) plots the RMSE against SNR, for the BSS-AIF method and the IQML with fixed, random, and ground-truth initializations. As the SNR increased, the RMSEs of both BSS-AIF and IQMLs decreased until it reached a stable state. IQML with fixed value initialization reduces to 0.18, and with random initialization 0.1. In contrast both BSS-AIF and IQML with ground truth initialization approached 0. In addition, the RMSE of BSS-AIF was smaller than both that of IQML with fixed initialization for SNR > 15 dB, and that of IQML with random initialization for SNR > 27 dB.

Figure 3 plots the estimated  $K^{trans}$ ,  $V_e$ , and  $V_p$  against the purities of the AIFs (assessment 3 in simulation B).

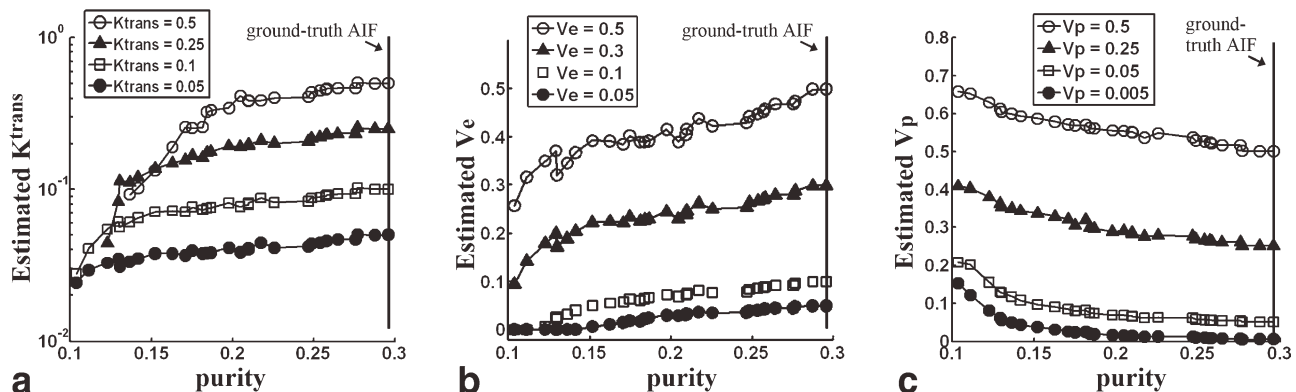


FIG. 3. Influence of purity of AIF (simulation B) to the estimated parameters. (a) The estimated  $K^{trans}$  (in logarithmic scale), (b)  $V_e$  (in linear scale), and (c)  $V_p$  (in linear scale) were plotted for various purities of AIFs. The vertical solid lines indicate the ground-truth AIF with maximum purity equal to 0.296.

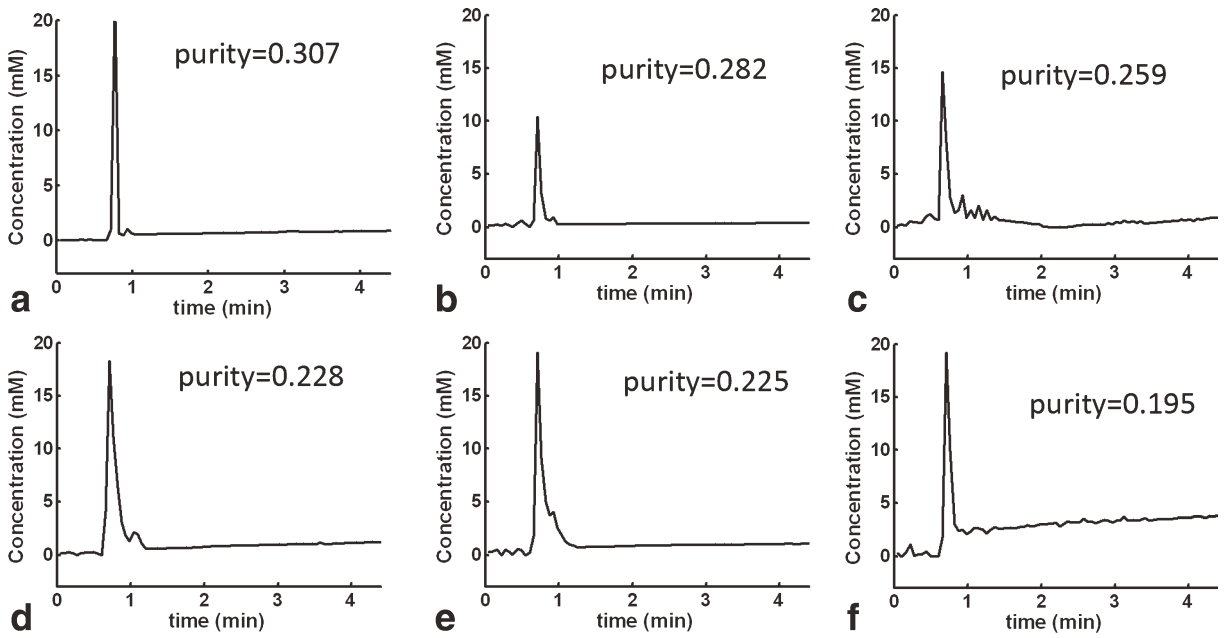


FIG. 4. Demonstration of the shapes of the manual- and BSS-AIFs. **a**: The BSS-AIF. **b-f**: The manually selected AIFs. The purities of manually selected AIFs were reduced, which could be attributed to either a decreased height of the peak (**b**), an elevated baseline of the curve (**c**), a broadening width in the first pass (**d,e**) or a drift of the returned baseline (**f**).

The ground-truth AIF (solid vertical lines) had the highest purity (0.296). As the purity increased, both  $K^{\text{trans}}$  and  $V_e$  increased while the  $V_p$  decreased. It was noticed that the tissues with high- $K^{\text{trans}}$  were more susceptible

to the purity, as indicated by the increased slope in Fig. 2a. The maximal differences in  $K^{\text{trans}}$ ,  $V_e$ , and  $V_p$  were 82%, 48%, and 24%, respectively, when the purity decreased from 0.296 to 0.104.

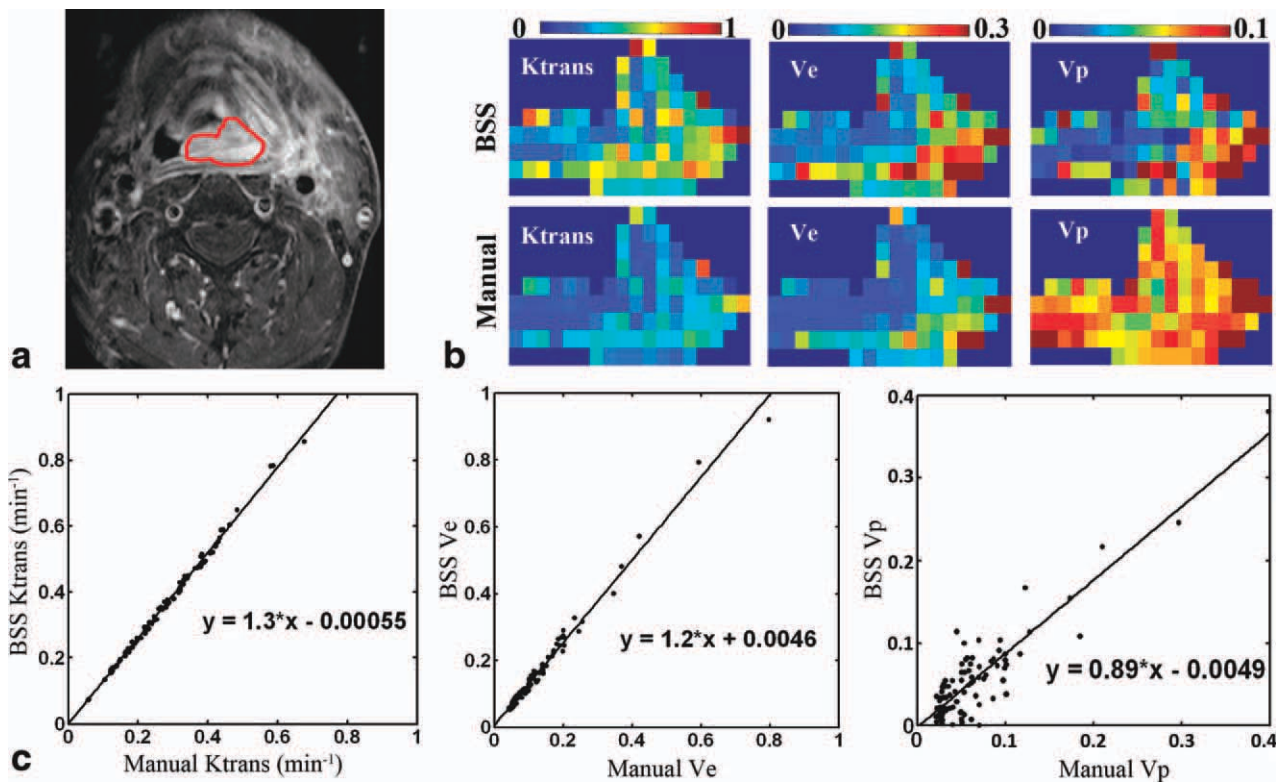


FIG. 5. Intraject comparison of kinetic parameters by using manual- and BSS-AIFs. **a**: Delineation of ROI on the tumor. **b**: A voxel-wise comparison of the kinetic parameters derived by using BSS-AIF (upper row) and manually selected AIF (lower row). **c**: Scatter plots of three derived parameters for voxels within the ROI (BSS-AIF versus manually selected AIF).

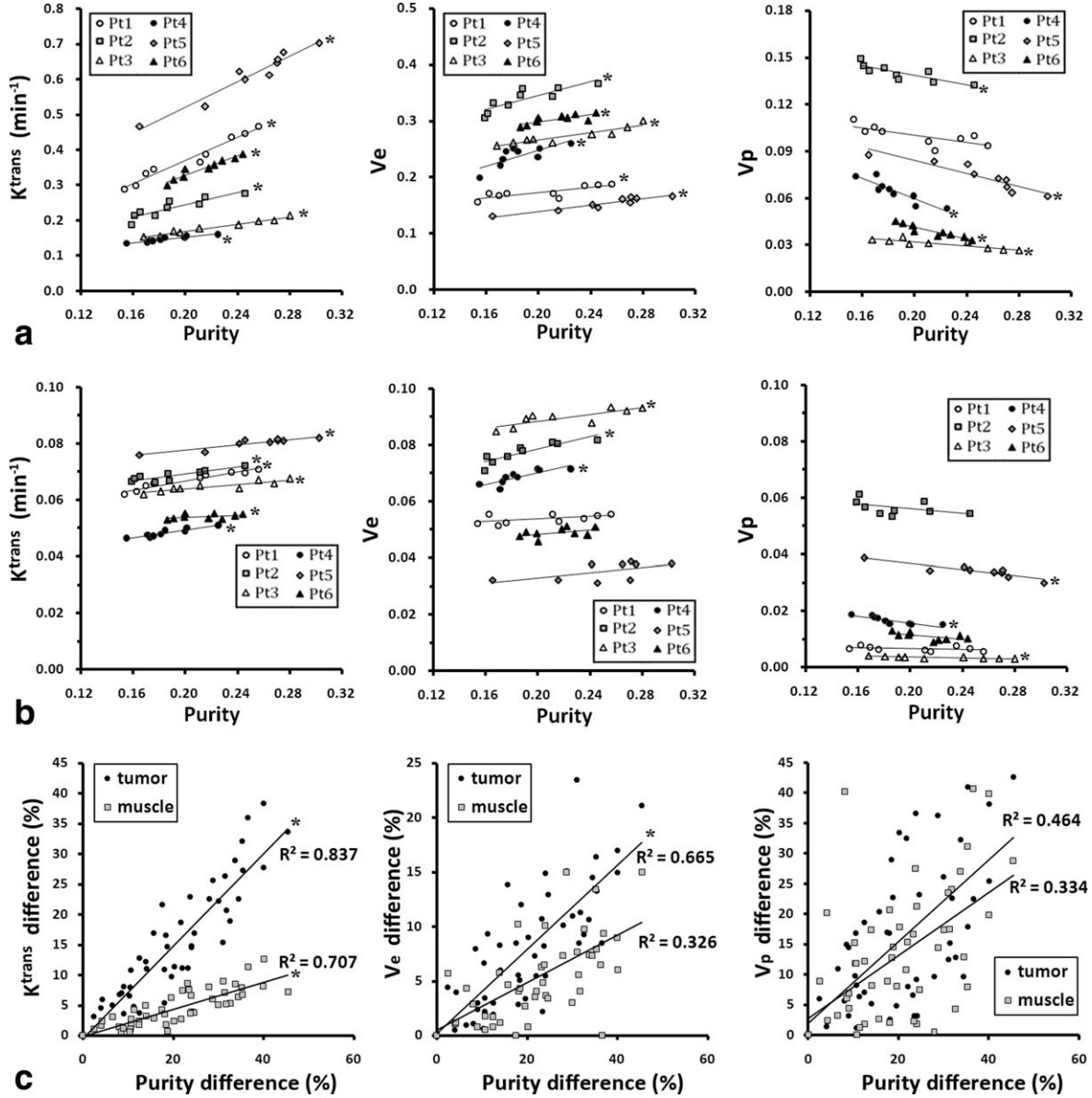


FIG. 6. Estimated parameters against the corresponding purities of AIFs from six patients. The  $K^{trans}$ ,  $V_e$ , and  $V_p$  were derived by using nine AIFs for each patient (eight manually selected AIFs and a BSS-AIF located at the highest purity for each patient). Evaluations were performed on the (a) tumor and (b) muscle of the patients. c: The percentage differences of the derived parameters were plotted against the difference of AIF purity. The symbols “\*\*” denote significant correlations with  $P < 0.05$ .

Figure 4 demonstrates the shapes of the manual- and BSS-AIFs. The shape of the concentration curve selected by BSS-AIF (a) is the sharpest. The purities of manually selected AIFs were reduced, which could be attributed to either a decreased height of the peak (b), an elevated baseline of the curve (c), a broadening width in the first pass (d,e), or a drift of the returned baseline (f).

Figure 5 shows the intrasubject comparison of the derived kinetic parameters by using manual- and BSS-AIFs in a representative patient. The ROI was delineated on the tumor for a voxel-wise comparison (Fig. 5a,b). The kinetic parameters derived from BSS-AIF from each voxel were plotted against those from the manual selection (Fig. 5c). It was noticed that both  $K^{trans}$  and  $V_e$  were higher while  $V_p$  of BSS-AIF was lower than those of

manually selected AIF (slopes of the regression lines = 1.3, 1.2, and 0.89 for  $K^{trans}$ ,  $V_e$ , and  $V_p$ , respectively). Pearson’s correlation showed a significant linear relationship between these two methods in all three parameters ( $P < 0.001$ ,  $r = 0.999$ ,  $0.993$ , and  $0.9017$  for  $K^{trans}$ ,  $V_e$ , and  $V_p$ , respectively).

Figure 6 plots the kinetic parameters against the purities of AIFs from the six patients. Nine AIFs were extracted from each patient, including eight manually selected and one BSS estimated. The BSS-estimated AIF had the highest purity. The kinetic parameters derived from the manually selected AIFs showed significant variations up to 38%, 23%, and 41% for  $K^{trans}$ ,  $V_e$ , and  $V_p$ , respectively, because of the difference in purities. All the BSS-AIFs were located in either carotid or vertebral

arteries (Supporting Information, S2 and S3). Both  $K^{\text{trans}}$ , and  $V_e$  were positively correlated to the purities of AIFs in all patients on both tumor and muscle. However, in  $V_e$  significant correlation in muscle was only found in three subjects. In contrast,  $V_p$  had significant negative correlations in five patients on tumor and three on muscle. Figure 6c plots the percentage differences of the derived parameters against the differences of purity in AIF. Significant correlations were found in  $K^{\text{trans}}$  (both tumor and muscle) and  $V_e$  (tumor). No correlations reach statistical significance in  $V_p$ . In all kinetic parameters, the lines of regression in the tumors had increased slopes than those of muscles.

Table 1 summarized the reproducibility of the derived kinetic parameters in the animal experiment using BSS- and manual-AIFs. No significant difference was found between  $T_{1_0}$  of the tumor obtained at the start of each injection ( $P = 0.221$ ). Shapiro–Wilk tests showed normal distribution in each parameter. Therefore, the reproducibility analysis was performed in the original scale [20]. No significant relationship between the absolute differences and means for each parameter (Kendall’s  $\tau$  test) was found, which indicated that the measurement error was independent of the magnitude of the parameter. The Wilcoxon’s-signed rank test showed no significant difference between the two scans in each parameter. It can be found that the within subject coefficient of variation for  $K^{\text{trans}}$  and  $V_e$  were improved using the BSS-AIF (0.075 and 0.137, respectively) than those by using manual AIF (0.106 and 0.205, respectively). The Bland–Altman plots of the repeatability analysis were shown in Figure 7. The repeatability levels of  $K^{\text{trans}}$  and  $V_e$  were lower by using the BSS-AIF (0.0122 and 0.0186, respectively) when compared with those by the manual AIF (0.0151 and 0.0237, respectively).

## DISCUSSION

In this study, we proposed an unsupervised BSS algorithm that could estimate the AIF from the voxel time course with the maximum purity. The identified AIF contained the least contamination from other tissues. Because the true AIF cannot be obtained in clinical practice, the proposed method provides the closest alternative choice. As the purity of the estimated AIF increased, the errors between the estimated AIF and the true one would reduce. The high purity in AIF can result in an improvement in the estimation of the derived pharmacokinetic parameters. In contrast, the conventional manually selected AIF had a reduced purity, which could lead to a significant variation in the derived index of interest.

Previous work indicated that the shape of AIF can be distorted in terms of peak amplitude, bolus width, and area under the curve by the partial volume effect [23]. The purity is a measure of the correlation between a function of interest to the impulse function, which is an ideal AIF. An AIF with a high purity is characterized by a rapid wash-in, rapid wash-out, a high amplitude of the peak, and a narrow width of the bolus. The simulation A suggests that the maximum purity provides a robust estimate of the AIF in all conditions when the partial vol-

Table 1  
Reproducibility Statistics of Derived Kinetic Parameters Using BSS-AIF and Manual-AIF in Rat Brain Tumors

Parameter	$K^{\text{trans}}$ (BSS)	$K^{\text{trans}}$ (manual)	$V_e$ (BSS)	$V_e$ (manual)	$V_p$ (BSS)	$V_p$ (manual)
Global mean ( $\pm$ SD)						
First injection	0.0564 $\pm$ 0.032	0.0515 $\pm$ 0.037	0.0489 $\pm$ 0.034	0.0440 $\pm$ 0.029	0.0125 $\pm$ 0.006	0.0137 $\pm$ 0.007
Second injection	0.0555 $\pm$ 0.033	0.0512 $\pm$ 0.033	0.0441 $\pm$ 0.028	0.0396 $\pm$ 0.027	0.0142 $\pm$ 0.007	0.0124 $\pm$ 0.009
Shapiro–Wilk normality test	0.909 ( $P = 0.344$ )	0.899 ( $P = 0.288$ )	0.947 ( $P = 0.679$ )	0.865 ( $P = 0.134$ )	0.905 ( $P = 0.318$ )	0.924 ( $P = 0.465$ )
Assessment of model assumptions						
Kendall’s $\tau$ test	–0.143 ( $P = 0.621$ )	0.071 ( $P = 0.805$ )	0.429 ( $P = 0.138$ )	0.071 ( $P = 0.805$ )	–0.143 ( $P = 0.621$ )	–0.143 ( $P = 0.621$ )
Wilcoxon’s-signed rank test	$P = 0.709$	$P = 0.889$	$P = 0.192$	$P = 0.208$	$P = 0.775$	$P = 0.674$
Reproducibility analysis						
Mean difference ( $\pm$ SD)	0.000862 $\pm$ 0.0063	0.000243 $\pm$ 0.0082	0.00452 $\pm$ 0.009	0.00449 $\pm$ 0.012	0.0017 $\pm$ 0.0048	0.00128 $\pm$ 0.0054
Square root of the mean squared difference	0.00592	0.0077	0.0095	0.01210	0.0048	0.0052
Within subject standard deviation	0.0044	0.005	0.0067	0.009	0.0037	0.0036
Repeatability ( $\alpha = 0.05$ )	0.0122	0.0151	0.0186	0.0237	0.0103	0.0102
Within subject coefficient of variation	0.075	0.106	0.137	0.205	0.274	0.282
Variance ratio	1.07 ( $P = 0.58$ )	0.97 ( $P = 0.65$ )	1.13 ( $P = 0.47$ )	1.03 ( $P = 0.51$ )	0.87 ( $P = 0.46$ )	0.85 ( $P = 0.41$ )

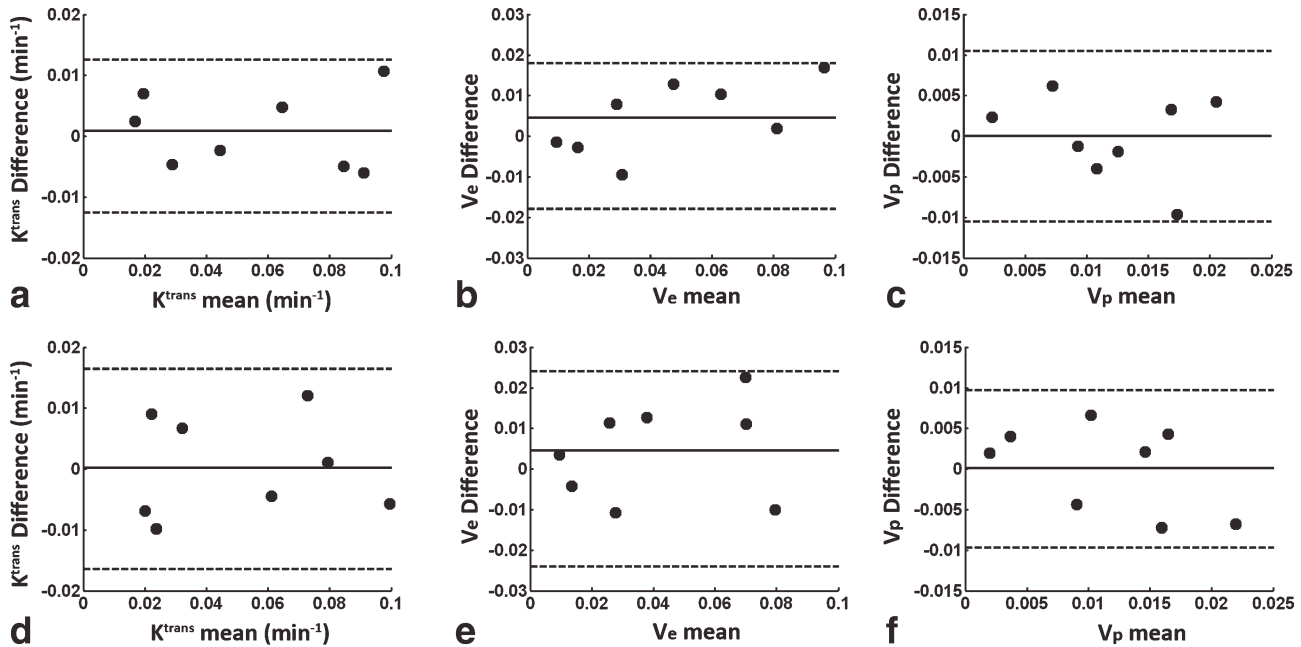


FIG. 7. Bland-Altman plots of the derived kinetic parameters of the tumor from eight rats. The kinetic parameters  $K^{\text{trans}}$ ,  $V_e$ , and  $V_p$  were derived by using BSS-AIF (a-c) and the manually selected AIF (d-f). The mean differences for each parameter are shown as the solid line, and the 95% limits of agreement are shown as the dotted lines.

ume effect is the minimum, i.e., when at either the highest  $V_p$ , lowest  $V_e$  or lowest  $K^{\text{trans}}$ . In contrast, both the peak height and the area under curve are not necessarily the best estimate of the AIF. In our clinical data, the shape of the AIF estimated by the BSS algorithm was the sharpest with the minimum distortion when compared with those by manually selected method.

The RMSE between the AIF from the proposed algorithm and the ground-truth reduced rapidly as the SNR increased (Fig. 2b). The measured SNR from *in vivo* data in the current study suggests that the performance of the BSS-AIF could be comparable with the IQML algorithm. Because the ground truth AIF is not always available, AIF identified by IQML can lead to significant variations in the derived pharmacokinetic parameters. Compared with the IQML algorithm, the BSS algorithm could provide a consistent estimation of the AIF independent of the given initial condition.

The derived  $K^{\text{trans}}$  and  $V_e$  were underestimated while  $V_p$  was overestimated in simulation, when the purity of the AIF was reduced. This observation was consistent with the image findings from the patients. In the same subject using the manual selection, reduction of both  $K^{\text{trans}}$  and  $V_e$  and increase of  $V_p$  were associated with a reduced purity. The Spearman's correlation indicated the same findings when compared among the subjects. The normalized differences in Fig. 6c indicated a positive dependence of the derived parameters on purity. The decreased purity could be related to a reduced arterial contribution. The estimated transfer constant may be underestimated due to the reduced arterial supply. The underestimation of extravascular volume,  $V_e$ , could be attributed to a limited contrast agent accumulation of a reduced transfer constant. This observation was consistent

with the overestimation in the plasma volume fraction,  $V_p$ .

The derived parameters of the tumor were more susceptible to the changes in purity than those of muscle (Fig. 6c), which could be related to the perfusion limited Kety model in tumor environment [17,18]. Both high-vascular permeability and insufficient blood flow in tumor lead to the dominance of the blood supply on the estimation of  $K^{\text{trans}}$ . In contrast, tissue microenvironment in muscle is permeability limited. Therefore, the  $K^{\text{trans}}$  is dominated by the permeability and surface area of the capillary wall, which are not affected by the fluctuations in blood supply. In addition, the vascular volume in normal muscle occupies only a small fraction of the total tissue volume. The effect of the fluctuations in the blood contribution  $c_p$  on the total tracer concentration  $x(i)$  is relatively restricted. Hence, the derived kinetic parameters in muscle are less affected by the changes in the purity of AIF. The findings have several implications in clinical studies, for example, in monitoring treatment response to cancer therapies. The manually selected AIF could lead to an underestimation in  $K^{\text{trans}}$  and  $V_e$  within the tumor environment, which in turn can result in a misinterpretation to the treatment efficacy because of the reduced observable changes.

The animal experiment showed good reproducibility in the derived kinetic parameters of the tumor by the BSS-AIF method. The reduced within subject coefficient of variation suggests that the BSS algorithm is robust when compared with the manual method. The lower repeatability level implies that a smaller change of  $K^{\text{trans}}$  and  $V_e$  in an individual could be considered to be statistically significant by using the BSS-AIF when compared with those by using the manual AIF. The interscan time

window in the reproducibility study was compromised between sufficient clearance of the contrast media and reduced physiological changes due to rapid tumor growth on the animal. Prolonged anesthesia could lead to unstable physiological state [24]. In the current study, the MR acquisitions were separated by durations longer than eight half lives of the contrast agent. During this period anesthesia was suspended to allow for animal recovery. Therefore, the voxel-by-voxel comparison was not available. However, the voxel-wise repeatability is not practical due to unavoidable motion from the animal, which results in interscan misregistration.

There are a few limitations in the present study. First, only the extended Kety model was adopted for the tracer kinetic modeling analysis. In the future, the effect of different kinetic models will be investigated. Second, the current study selected the pixel with the highest purity. A potential risk is that the choice could suffer from the poor SNR. The use of an average from multiple voxels could alleviate the issue but will unfortunately reduce the purity due to partial volume effect. In the future, it will be assessed whether an average of multiple voxels with high purities will improve the estimation efficiency when in data with low SNR. Third, if there are no arterial voxels in the data set that are free from partial volume effects, then the BSS AIF will produce biased estimates of the tracer kinetic parameters. The lack of information related to the AIF in the data set could lead to failure in most AIF identification techniques. Technically, in a clinical dataset, an arterial voxel is usually included within the three-dimensional volume. The BSS algorithm can automatically search this volume and find the AIF with a relatively higher purity, which may be difficult to identify visually when using the manual method.

In conclusion, an automatic AIF estimation method was proposed. The voxel with the maximum purity can be identified in the mixed tissue. The extracted AIF is closest to the ground-truth one. The derived pharmacokinetic parameters are consistently reproducible.

## ACKNOWLEDGMENTS

The MRI facilities were supported by Molecular Imaging Center, Chang Gung Memorial Hospital, Linkou.

## APPENDIX A

Consider the signal model given by Eq. 2

$$\mathbf{x}(i) = [\mathbf{B}(i)\mathbf{c}_p \quad \mathbf{c}_p] \begin{bmatrix} K^{\text{trans}}(i) \\ V_p(i) \end{bmatrix}, \quad [\text{A1}]$$

where

$$\mathbf{B}(i) = \Delta t$$

$$\times \begin{bmatrix} 1 & 0 & \dots & 0 \\ \exp[-k_{\text{ep}}(i)(t_2 - t_1)] & 1 & & 0 \\ \vdots & \vdots & \ddots & \vdots \\ \exp[-k_{\text{ep}}(i)(t_K - t_1)] & \exp[-k_{\text{ep}}(i)(t_K - t_2)] & \dots & 1 \end{bmatrix}.$$

Since the elements in  $\mathbf{x}(i)$  are non-negative, the purity measure can also be written as

$$\rho_i = \left\| \frac{\mathbf{x}(i)}{\mathbf{1}^T \mathbf{x}(i)} \right\|_2 = \left\| \bar{s}_1(i) \left( \frac{\mathbf{B}(i)\mathbf{c}_p}{\mathbf{1}^T \mathbf{B}(i)\mathbf{c}_p} \right) + \bar{s}_2(i)\bar{\mathbf{c}}_p \right\|_2, \quad [\text{A2}]$$

where  $\bar{s}_1(i) = K^{\text{trans}}(i)\mathbf{1}^T \mathbf{B}(i)\mathbf{c}_p / \mathbf{1}^T \mathbf{x}(i)$ ,  $\bar{s}_2(i) = V_p(i)\mathbf{1}^T \mathbf{c}_p / \mathbf{1}^T \mathbf{x}(i)$ ,  $\bar{\mathbf{c}}_p = \mathbf{c}_p / \mathbf{1}^T \mathbf{c}_p$ , and  $\mathbf{1}$  is an all-one vector. It is also easy to verify that  $\bar{s}_1(i) + \bar{s}_2(i) = 1$  and  $\bar{s}_1(i) \geq 0$ ,  $\bar{s}_2(i) \geq 0$ . In addition, since the purity measure is also a sparsity measure [25],  $\mathbf{c}_p$  convolved with the smooth finite impulse response such as  $\mathbf{B}(i)$  for  $k_{\text{ep}}(i) \geq 0$  will decrease the sparsity of  $\mathbf{c}_p$ , i.e.,

$$\left\| \frac{\mathbf{B}(i)\mathbf{c}_p}{\mathbf{1}^T \mathbf{B}(i)\mathbf{c}_p} \right\|_2 \leq \left\| \frac{\mathbf{c}_p}{\mathbf{1}^T \mathbf{c}_p} \right\|_2 = \|\bar{\mathbf{c}}_p\|_2. \quad [\text{A3}]$$

Therefore, by Eqs. A2 and A3, and Jensen's inequality, we have

$$\begin{aligned} \rho_i &\leq \bar{s}_1(i) \left\| \frac{\mathbf{B}(i)\mathbf{c}_p}{\mathbf{1}^T \mathbf{B}(i)\mathbf{c}_p} \right\|_2 + \bar{s}_2(i) \left\| \frac{\mathbf{c}_p}{\mathbf{1}^T \mathbf{c}_p} \right\|_2 \\ &\leq \max \left\{ \left\| \frac{\mathbf{B}(i)\mathbf{c}_p}{\mathbf{1}^T \mathbf{B}(i)\mathbf{c}_p} \right\|_2, \left\| \frac{\mathbf{c}_p}{\mathbf{1}^T \mathbf{c}_p} \right\|_2 \right\} \leq \|\bar{\mathbf{c}}_p\|_2, \end{aligned}$$

where the equality holds if and only if  $i$  is such that  $\bar{s}_2(i) = 1$  and  $\bar{s}_1(i) = 0$ . Hence, assuming the presence of artery in the DCE-MR images (i.e., there exists a pure arterial voxel index  $\ell$  such that  $V_p(\ell) = 1$  and  $K^{\text{trans}}(\ell) = 0$ , which leads to  $\mathbf{x}(\ell) = \mathbf{c}_p$ ), then selecting the voxel with the maximum purity measure

$$i^* = \arg_i \max \rho_i$$

would identify the voxel which is fully contributed from AIF, i.e.,  $i^* = \ell$ .

## APPENDIX B

The IQML method is summarized as follows. By Eq. A1, Eq. 2 can also be expressed as

$$\mathbf{x}(i) = (K^{\text{trans}}(i)\mathbf{B}(i) + V_p(i)\mathbf{I})\mathbf{c}_p, i = 1, \dots, L$$

where  $\mathbf{I}$  is a  $K \times K$  identity matrix, and  $L$  is the number of voxels in DCE-MRI data cube. Stacking matrices on top of each other, we get a linear system of equations

$$\begin{aligned} \mathbf{y} = \begin{bmatrix} \mathbf{x}(1) \\ \vdots \\ \mathbf{x}(L) \end{bmatrix} &= \begin{bmatrix} K^{\text{trans}}(1)\mathbf{B}(1) + V_p(1)\mathbf{I} \\ \vdots \\ K^{\text{trans}}(L)\mathbf{B}(L) + V_p(L)\mathbf{I} \end{bmatrix} \mathbf{c}_p \\ &= \mathbf{H}(\{K^{\text{trans}}(i), k_{\text{ep}}(i), V_p(i)\}_{i=1}^L) \mathbf{c}_p. \end{aligned}$$

where

$$\mathbf{H}(\{K^{\text{trans}}(i), k_{\text{ep}}(i), V_p(i)\}_{i=1}^L) = \begin{bmatrix} K^{\text{trans}}(1)\mathbf{B}(1) + V_p(1)\mathbf{I} \\ \vdots \\ K^{\text{trans}}(L)\mathbf{B}(L) + V_p(L)\mathbf{I} \end{bmatrix}$$

is a function of kinetic parameters  $\{K^{\text{trans}}(i), k_{\text{ep}}(i)\}_{i=1}^L$  and plasma volume,  $\{V_p(i)\}_{i=1}^L$ . IQML is to find  $\{K^{\text{trans}}(i), k_{\text{ep}}(i), V_p(i)\}_{i=1}^L$  and  $\mathbf{c}_p$  together by handling the least squares problem:

$$\min_{\{K^{\text{trans}}(i), k_{\text{ep}}(i), V_p(i)\}_{i=1}^L, \mathbf{c}_p} \left\| \mathbf{y} - \mathbf{H} \left( \{K^{\text{trans}}(i), k_{\text{ep}}(i), V_p(i)\}_{i=1}^L \right) \mathbf{c}_p \right\|_2$$

which is equivalent to

$$\min_{\{K^{\text{trans}}(i), k_{\text{ep}}(i), V_p(i)\}_{i=1}^L} \left\| \mathbf{P}_{\mathbf{H}}^{\perp} \left( \{K^{\text{trans}}(i), k_{\text{ep}}(i), V_p(i)\}_{i=1}^L \right) \mathbf{y} \right\|_2,$$

where  $\mathbf{P}_{\mathbf{H}}^{\perp} = \mathbf{I} - \mathbf{H}(\mathbf{H}^T \mathbf{H})^{-1} \mathbf{H}^T$  is the orthogonal complement projector of  $\mathbf{H}$ . The above nonconvex problem can be handled by any nonlinear program solver, but the solution found could be subject to a local optimality issue depending on the initial point provided. Once a solution  $\{K^{\text{trans}'}(i), k_{\text{ep}'}(i), V_p'(i)\}_{i=1}^L$  is obtained, the estimated AIF is given by

$$\hat{\mathbf{c}}_p = \mathbf{H} \left( \{K^{\text{trans}'}(i), k_{\text{ep}'}(i), V_p'(i)\}_{i=1}^L \right)^{\dagger} \mathbf{y},$$

where  $\mathbf{H}^{\dagger} = (\mathbf{H}^T \mathbf{H})^{-1} \mathbf{H}^T$ .

## REFERENCES

1. Yuh WT, Mayr NA, Jarjoura D, Wu D, Grecula JC, Lo SS, Edwards SM, Magnotta VA, Sammet S, Zhang H, Montebello JF, Fowler J, Knopp MV, Wang JZ. Predicting control of primary tumor and survival by DCE MRI during early therapy in cervical cancer. *Invest Radiol* 2009;44:343–350.
2. Sorensen AG, Batchelor TT, Zhang WT, Chen PJ, Yeo P, Wang M, Jennings D, Wen PY, Lahdenranta J, Ancukiewicz M, di Tomaso E, Duda DG, Jain RK. A “vascular normalization index” as potential mechanistic biomarker to predict survival after a single dose of cediranib in recurrent glioblastoma patients. *Cancer Res* 2009;69:5296–5300.
3. Beaumont M, DuVal MG, Loai Y, Farhat WA, Sandor GK, Cheng HL. Monitoring angiogenesis in soft-tissue engineered constructs for calvarium bone regeneration: an in vivo longitudinal DCE-MRI study. *NMR Biomed* 2010;23:48–55.
4. Singh A, Rathore RK, Haris M, Verma SK, Husain N, Gupta RK. Improved bolus arrival time and arterial input function estimation for tracer kinetic analysis in DCE-MRI. *J Magn Reson Imaging* 2009;29:166–176.
5. Cron GO, Footitt C, Yankeelov TE, Avruch LI, Schweitzer ME, Cameron I. Arterial input functions determined from MR signal magnitude and phase for quantitative dynamic contrast-enhanced MRI in the human pelvis. *Magn Reson Med* 2011;66:498–504.
6. Just N, Koh DM, D’Arcy J, Collins DJ, Leach MO. Assessment of the effect of haematocrit-dependent arterial input functions on the accuracy of pharmacokinetic parameters in dynamic contrast-enhanced MRI. *NMR Biomed* 2011;24:902–915.
7. Bleeker EJ, van Osch MJ, Connelly A, van Buchem MA, Webb AG, Calamante F. New criterion to aid manual and automatic selection of the arterial input function in dynamic susceptibility contrast MRI. *Magn Reson Med* 2011;65:448–456.
8. Roberts C, Little R, Watson Y, Zhao S, Buckley DL, Parker GJ. The effect of blood inflow and B(1)-field inhomogeneity on measurement of the arterial input function in axial 3D spoiled gradient echo dynamic contrast-enhanced MRI. *Magn Reson Med* 2011;65:108–119.
9. Buckley DL. Uncertainty in the analysis of tracer kinetics using dynamic contrast-enhanced T1-weighted MRI. *Magn Reson Med* 2002;47:601–606.
10. Parker GJ, Roberts C, Macdonald A, Buonaccorsi GA, Cheung S, Buckley DL, Jackson A, Watson Y, Davies K, Jayson GC. Experimentally-derived functional form for a population-averaged high-temporal-resolution arterial input function for dynamic contrast-enhanced MRI. *Magn Reson Med* 2006;56:993–1000.
11. Yang C, Karczmar GS, Medved M, Stadler WM. Estimating the arterial input function using two reference tissues in dynamic contrast-enhanced MRI studies: fundamental concepts and simulations. *Magn Reson Med* 2004;52:1110–1117.
12. Yang C, Karczmar GS, Medved M, Stadler WM. Multiple reference tissue method for contrast agent arterial input function estimation. *Magn Reson Med* 2007;58:1266–1275.
13. Yankeelov TE, Luci JJ, Lepage M, Li R, Debusk L, Lin PC, Price RR, Gore JC. Quantitative pharmacokinetic analysis of DCE-MRI data without an arterial input function: a reference region model. *Magn Reson Imaging* 2005;23:519–529.
14. Calamante F, Morup M, Hansen LK. Defining a local arterial input function for perfusion MRI using independent component analysis. *Magn Reson Med* 2004;52:789–797.
15. Riabkov DY, Di Bella EV. Estimation of kinetic parameters without input functions: analysis of three methods for multichannel blind identification. *IEEE Trans Biomed Eng* 2002;49:1318–1327.
16. Fluckiger JU, Schabel MC, Dibella EV. Model-based blind estimation of kinetic parameters in dynamic contrast enhanced (DCE)-MRI. *Magn Reson Med* 2009;62:1477–1486.
17. Tofts PS, Brix G, Buckley DL, Evelhoch JL, Henderson E, Knopp MV, Larsson HB, Lee TY, Mayr NA, Parker GJ, Port RE, Taylor J, Weisskoff RM. Estimating kinetic parameters from dynamic contrast-enhanced T(1)-weighted MRI of a diffusable tracer: standardized quantities and symbols. *J Magn Reson Imaging* 1999;10:223–232.
18. Kety SS. The theory and applications of the exchange of inert gas at the lungs and tissues. *Pharmacol Rev* 1951;3:1–41.
19. Schabel MC, Parker DL. Uncertainty and bias in contrast concentration measurements using spoiled gradient echo pulse sequences. *Phys Med Biol* 2008;53:2345–2373.
20. Padhani AR, Hayes C, Landau S, Leach MO. Reproducibility of quantitative dynamic MRI of normal human tissues. *NMR Biomed* 2002;15:143–153.
21. Bland JM, Altman DG. Measuring agreement in method comparison studies. *Stat Methods Med Res* 1999;8:135–160.
22. Bland JM, Altman DG. Measurement error and correlation coefficients. *BMJ* 1996;313:41–42.
23. Kjolby BF, Mikkelsen IK, Pedersen M, Ostergaard L, Kiselev VG. Analysis of partial volume effects on arterial input functions using gradient echo: a simulation study. *Magn Reson Med* 2009;61:1300–1309.
24. Yankeelov TE, DeBusk LM, Billheimer DD, Luci JJ, Lin PC, Price RR, Gore JC. Repeatability of a reference region model for analysis of murine DCE-MRI data at 7T. *J Magn Reson Imaging* 2006;24:1140–1147.
25. Hurley N and Rickard S. Comparing measures of sparsity. *IEEE Trans Inf Theory* 2009;55:4723–4741.